


## Characterizing energy dissipation of shallow-water wave breaking in a storm surge

Hunter Boswell \*

*Department of Mechanical and Aerospace Engineering, Missouri University of Science and Technology, Toomey Hall, 400 W. 13th Street, Rolla, Missouri 65409-0050, USA*

Guirong Yan †

*Department of Civil, Architectural, and Environmental Engineering, Missouri University of Science and Technology, Butler-Carlton Hall, 1401 N. Pine Street, Rolla, Missouri 65409-0030, USA*

Wouter Mostert ‡

*Department of Engineering Sciences, University of Oxford, Parks Road, Oxford OX1 3PJ, United Kingdom*



(Received 30 September 2022; accepted 28 March 2023; published 5 May 2023)

While understanding breaking waves is crucial for the development of parametrizations used in ocean wave modeling for both deep and shallow water, the complete process of wave breaking is not well understood. Here we present direct numerical simulations of two-dimensional solitary waves that shoal and break on a uniform beach in shallow water, with the presence of storm surge represented by an inshore region. The storm surge depth, beach slope, and wave amplitude are varied to study the dependence of energy dissipation in the breaker on wave and bathymetric parameters. We classify wave breaker types and find a separation between plunging and spilling breakers when scaled by breaking amplitude and depth. We compare energy dissipation during the breaking process with results from the literature without storm surge. A representation of energy dissipation in this solitary wave breaker data is also compared with prior experiments and simulations of breakers in deep water, and possibilities of a unifying model are explored. We conclude that a previously developed shallow-water inertial dissipation model for wave breaking on a uniform slope can be extended to this storm surge environment with good data collapse, and we further discuss possibilities for a general parametrization of wave breaking valid across different depth regimes.

DOI: [10.1103/PhysRevFluids.8.054801](https://doi.org/10.1103/PhysRevFluids.8.054801)

### I. INTRODUCTION

As water waves approach a beach or shore, they steepen and break, dissipating the energy that they have gained in generation processes that occur well away from the shore. Given that the impact of coastal storms on the built environment has become more severe in recent years owing to climate change and increased urban development, there has been an increasingly urgent need to understand the loadings that such breaking waves exert on coastal and offshore infrastructure, particularly in the presence of other storm-related phenomena, such as strong winds and storm surge [1]. There is also a fundamental interest in breaking waves: deep water breakers modulate mass, momentum, and

---

\*hcbxtd@mst.edu

†yang@mst.edu

‡wouter.mostert@eng.ox.ac.uk

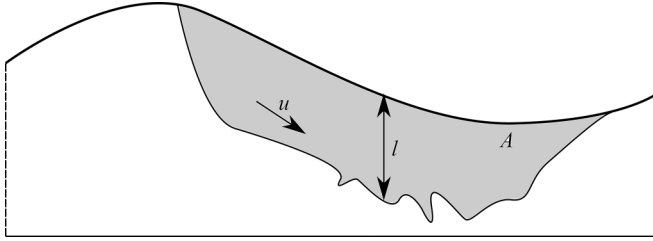


FIG. 1. Turbulent zone formed by the wave after breaking, showing the relevant integral velocity scale  $u$ , length scale  $l$ , and cross-sectional area  $A$ . The relationship between these scales and the wave parameters is unchanged between deep and shallow water, except for  $l$ . Adopted from [46] [Fig. 1(c)].

energy transfer between the ocean and the atmosphere [2], while in the nearshore environment they play a strong role in dissipating wave energy [3–5], the development of currents [3,5–7], runup and setup of the shoreline water level [3,6,8], and transport of sediment and biological material via turbulent dissipation [7,9]. A physical understanding of these phenomena is crucial for the development of robust parametrizations used in modeling wave systems and, ultimately, the dynamics of the ocean and atmospheric processes [1].

Although the shallow-water wave breaking process has been studied for many years, its complete understanding remains elusive. To study the fundamental dynamics of shoaling breakers, simplified bathymetries such as uniform slopes or step transitions in depth are often utilized. The problem of wave propagation into an inundated area (such as by storm surge) may be modeled by a change in depth with a linear slope transition (see Fig. 2 below); the dynamics of individual breakers may then be clearly examined by the propagation of a solitary wave over such a bathymetry. Such a problem has not to our knowledge been extensively investigated, aside from an analytical examination conducted by Bautista *et al.* [10]. In fact, most investigations have considered a uniform beach without an inshore inundated region [11–20], an abrupt change in depth, such as over a bathymetric shelf [21–27], or a submerged breakwater [28,29].

Configurations such as these are useful for gaining an understanding of the small-scale physics of wave propagation, steepening, and breaking; this understanding can then be used to improve larger-scale modeling efforts. Aside from experimental methods, a variety of wave-resolving numerical models and tools have been used to understand these simple systems. Large-eddy simulation is used for understanding phenomena at and above the individual wave scale but relies on assumptions for the small-scale processes involving turbulence and void-fraction effects. Fully nonlinear potential flow models [19,30] are especially powerful for understanding the evolution of prebreaking waves but cannot capture the breaking process itself or the associated dissipative processes. However, with

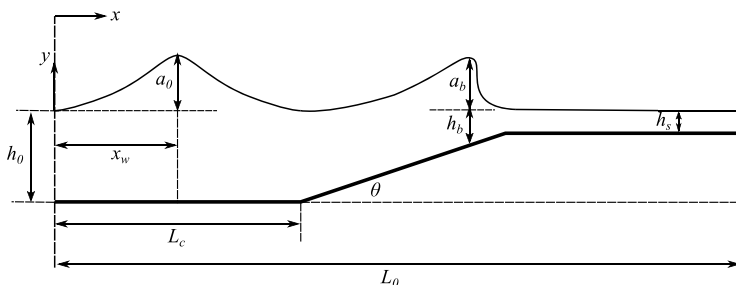


FIG. 2. Schematic diagram of wave breaking process. Conditions are shown at initialization and at point of breaking. When the wave breaks, the leading interface of the wave becomes vertical, and the wave amplitude  $a_b$  is measured at this instant.

increasing sophistication of numerical methods and availability of computational resources, it has become possible in recent years to use direct numerical simulation (DNS) in simulating the wave breaking process [20,31–35]. While the main drawback of DNS is that it is too computationally expensive to simulate intermediate- or large-scale wave systems, DNS of wave breaking nevertheless provides a powerful investigative tool for understanding the small-scale physics of breakers directly. Somewhat surprisingly, this has proven the case even for two-dimensional (2D) simulations, despite the essentially three-dimensional (3D) character of turbulence: many investigations by different authors across a variety of different experimental and numerical setups have shown that 2D numerical breakers experience dissipation rates very similar to 3D numerical and experimental breakers [33–36], although naturally slightly smaller; this remains the topic of ongoing investigation [35]. On the basis of these observations, and following [20], we will assume here that 2D simulations are a reasonable proxy for the energetic dissipation of the full 3D simulations, subject to confirmation in a future study.

The purpose of the present study is to perform DNS of a breaking solitary wave on a simple bathymetry in the presence of a storm surge. The resulting data will then be used to set up physics-informed parametrizations for wave energy dissipation in storm surge conditions, for future applications to larger-scale models that operate under more realistic topographies and bathymetries, such as Simulating WAVes Nearshore (SWAN). We will present 2D DNS of solitary breakers approaching an inundated beach with a configuration shown in Fig. 2. Solitary waves have long been used as models for studying breaking processes (e.g., [11,12,37]). In this study we will include an inundated inshore beach region, which allows the broken wave to propagate over a region of uniform depth. In the course of the analysis, the generality of parametrizations and relevance of scaling arguments usually applied to deep-water systems will also be discussed.

The remainder of this paper is organized as follows. In Sec. II a brief review is provided on some existing physics-based parametrizations for energy dissipation in breaking waves, which will be tested against new data in Sec. IV. In Sec. III the problem itself is formulated and the methodology presented. Next in Sec. IV we present the data, test the various parametrizations against it, and discuss insights that may lead to a general water-depth-independent parametrization. Finally, in Sec. V conclusions are drawn, and future work is suggested.

## II. REVIEW ON MODEL PARAMETRIZATIONS FOR WAVE BREAKING

The present study centers on the use of DNS to generate high-resolution data that can inform the development of strictly physics-informed parametrizations for wave breaking in shallow water. Therefore, in this section we briefly discuss some existing physics-based parametrizations relying on geometric and dynamic considerations of local wave properties. Pictorial representations of the wave breaking process relevant to this study are shown in Figs. 1 and 2. There are many breaker models besides the ones discussed below, including the roller model [38], which makes extensive use of Duncan’s [39,40] observations, or the eddy viscosity approach [41], but these will not be discussed here.

First, following Duncan [39] and Phillips [42], energy dissipation in breakers is often expressed in terms of the dimensionless  $b$  parameter,

$$b = \frac{g\epsilon_l}{\rho c^5}, \quad (1)$$

owing, among other things, to its utility in expressing energy dissipation in a wave system as the fifth moment of Phillips’ wave breaking distribution,  $\Lambda(\mathbf{c})$ . Here  $\epsilon_l$  is the (dimensional) energy dissipation rate per unit length of breaking crest,  $\mathbf{c}$  is the velocity of the breaking crest,  $\rho$  is the water density, and  $g$  is gravitational acceleration. The key observation is that the dissipation rates in geometrically similar breakers are proportional to the fifth power of the crest speed  $c = |\mathbf{c}|$ . The dependence of the proportionality parameter  $b$  has seen several studies of its dependence on the breaker geometry since its introduction in [39].

One of the oldest approaches to characterizing breaker dissipation, particularly in shallow water, is to model breaking waves as being energetically equivalent to hydraulic jumps. The dissipation rate of a hydraulic jump in shallow water is easily derived from applying a conservation analysis on the nonlinear shallow-water equations (NLSWEs) [43] and given by

$$\epsilon_l = \frac{\rho g}{4} \left( \frac{g(h_2 + h_b)}{2h_b h_2} \right)^{1/2} (h_2 - h_b)^3, \quad (2)$$

where  $h_b$  and  $h_2$  are the water depth ahead of and behind the hydraulic jump, respectively. This model is, for example, used to set the energy dissipation in the “shock-capturing” approach of certain joint Boussinesq-NLSWE models [44], as well as in third-generation spectral wave models such as SWAN [45].

Inertial arguments for breaker properties have also been developed in deep [46] and shallow water [20] as a function of the breaker’s geometric properties. They use the same dimensional-analytical approach to develop their dissipation scaling arguments. The difference between them arises solely from the integral length scale of the eddies in the turbulent zone formed by the breaker (see Fig. 1). Namely, under Taylor’s hypothesis, the local turbulent dissipation rate is given by  $\epsilon = u^3/l$ : according to [20] and [46], in both shallow and deep water,  $u \simeq \sqrt{2ga_b}$ ; in deep water  $l \propto a_b$  [46], which reflects the length scale at which energy is input into the turbulent zone, while in shallow water  $l \propto h_b$ , since often  $h_b \leq a_b$  and eddies with a diameter larger than the local depth cannot exist [20]. The dissipation rate per unit length of breaking crest is related to the turbulent dissipation rate by  $\epsilon_l = \rho A \epsilon$ , where the area of the turbulent zone is assumed to be cylindrical such that  $A = \pi a_b^2/4$ . This leads to the scalings

$$\epsilon_l = \beta_1 \rho g^{3/2} a_b^{5/2}, \quad b \propto S^{5/2} \quad (3)$$

in deep water, where  $S$  is the local slope parameter of the breaker [46], and

$$\frac{\epsilon_l}{\rho g^{3/2} h_0^{5/2}} = \beta_2 \left( \frac{a_b}{h_0} \right)^{7/2} \left( \frac{h_b}{h_0} \right)^{-1}, \quad (4)$$

$$\epsilon_l = \beta_2 \rho g^{3/2} \frac{a_b^{7/2}}{h_b}, \quad b \propto (a_b/h_b)^{7/2} \quad (5)$$

in shallow water [20], where  $a_b$  is the wave amplitude at breaking and  $h_b$  is the water depth immediately ahead of the breaker, and  $\beta_1, \beta_2$  are both dimensionless constants. Using appropriate semiempirical fits to draw together a variety of data sets [47], the deep-water model in particular has proved very successful for use in spectral wave modeling in the open ocean ([47,48]) and in its fundamental form has even been shown to perform slightly better than the hydraulic jump model in an inner surf zone problem (e.g., [49]). While very similar in formulation, the deep- and shallow-water models were applied to different environments. That is, the deep-water model of [46] was applied to study dispersively focused wave packets, while the shallow-water model of [20] was applied to study shoaling solitary waves. Nevertheless, this approach is agnostic of the origin of the breaker of interest, as it considers only local geometric parameters at the point of breaking. These inertial models are what we will primarily compare in this study. Note that Pizzo *et al.* and Sinnis *et al.* [50,51] proposed a modification of the inertial model of [46] for deep-water-focused packets by interpreting the cross-sectional area of the breaker in terms of a wave-number bandwidth. However, this work will not be directly incorporated in the present study given the difficulty of defining wavelength [16] (or indeed bandwidth) for solitary waves. Finally, the model of Derakhti *et al.* [18] relays a dynamic criterion [52] for a breaking threshold, finding collapse of their breaker dissipation rates by using the semiempirical scaling,  $b = 0.034(\Gamma - 0.30)^{5/2}$ ,  $\Gamma = T_b dB/dt|_{B_{th}}$ , where  $B = u_x/c$  is the particle speed at the crest relative to the crest speed,  $B_{th} = 0.85$  is the threshold value of  $B$  taken as a criterion for breaking and  $T_b$  is the period of the carrier wave. Although developed for breakers in deep and intermediate water, this model may also in principle

TABLE I. Values of  $\Delta x/a_0$  for associated  $a_0/h_0$ .

$a_0/h_0$	0.2	0.3	0.4	0.5
$\Delta x/a_0$	1/32.7	1/49.1	1/65.5	1/81.9

be applicable to shallow water or solitary waves, but owing to difficulties in the measurement of  $\Gamma$  in the present data (see Sec. IV E), we will not directly compare this parametrization.

### III. FORMULATION AND METHODOLOGY

#### A. Numerical method

For the simulations used in this study, we use the Basilisk package, an open-source numerical library, developed as a successor to the Gerris Flow Solver, to solve partial differential equations on regular adaptive Cartesian meshes [53]. Following [20], we use Basilisk to solve the nonlinear incompressible Navier-Stokes equations in two phases (air and water) with variable density and surface tension. In this solver, the Bell-Colella-Graz projection method [54] is used to solve the momentum equation, and a momentum-conservative volume of fluid (VOF) advection scheme is used to advect the liquid-gas boundary, which helps to maintain a relatively sharp interface representation [55]. The method of [56], which was further developed and implemented by [55], is used to model the surface tension.

The incompressible Navier-Stokes equations with surface tension and variable density govern the flow in the two phases (water and air) and can be written as

$$\begin{cases} \rho(\partial_t \mathbf{u} + (\mathbf{u} \cdot \nabla) \mathbf{u}) = -\nabla p + \nabla \cdot (2\mu \mathbf{D}) + \gamma \kappa \delta_s \mathbf{n} \\ \partial_t \rho + \nabla \cdot (\rho \mathbf{u}) = 0 \\ \nabla \cdot \mathbf{u} = 0 \\ \frac{\partial f}{\partial t} + \mathbf{u} \cdot \nabla f = 0 \end{cases}, \quad (6)$$

where  $\mathbf{u} = (u, v)$  is the fluid velocity,  $\rho$  the density,  $\mu$  the dynamic viscosity, and  $\mathbf{D}$  the deformation tensor. The interface between air and water is defined by the  $\gamma \kappa \delta_s \mathbf{n}$  term, where  $\delta_s$  is the Dirac delta function,  $\gamma$  is surface tension, and  $\kappa$  and  $\mathbf{n}$  are the mean curvature and normal of the interface, respectively, which are estimated using a height function approach in the VOF scheme [55]. The volume of fluid tracer  $f$  is used to distinguish between air and water phases, and sets the density and viscosity in the relevant phase.

The Basilisk software library features a quadtree-based adaptive mesh refinement (AMR) scheme, which allows high effective resolutions to be attained at a fraction of computational cost associated with conventional, uniform-grid approaches [53,57]. The method identifies and finely resolves only the active portions of the simulated flow, while using coarser local resolutions for roughly quiescent regions. In particular, the AMR approach more easily allows the direct resolution of small-scale turbulence in water without the need of a turbulence model. The criterion for refinement is determined through a wavelet algorithm, which estimates the discretization error in the velocity and VOF fields, following [20,35].

In this study, effective resolutions are stated in terms of the level parameter  $Le$ , where  $x = L_0/(2^{Le})$  is the minimum grid size and  $L_0$  is the domain length. The maximum resolution is set to  $Le = 13$  for the cases presented here; numerical convergence of the energy budgets, which are used to determine energy dissipation, is shown in Appendix A.

For all simulations, the bathymetry length was set to  $L_0/h_0 = 50$ . We have  $\Delta x/L_0 = 1/2^{13}$  and  $\Delta x/L_c = 1/1638.4$ , where  $L_c = 10h_0$ . For the viscous boundary layer, we use Batchelor's estimate,  $\delta_v \sim h_0/\sqrt{Re} = 5 \times 10^{-3}h_0$ . So we have  $\Delta x/\delta_v = 1/(5 \times 10^{-3}h_0)$ . For the capillary length scale, we have  $\Delta x/\lambda_c = 3.67 \text{ cm}^{-1}$  (although for this 2D study we do not consider bubbles or droplets).

Additionally, several values of  $\Delta x/a_0$  are shown in Table I for various values of  $a_0/h_0$ . The maximum resolution is 16 cells over the wave amplitude.

### B. Problem formulation

We consider a varying bathymetry, featuring a depth change with a linear transition, as illustrated in Fig. 2, as a simple model for wave runup in conditions of a storm surge. After some distance,  $L_c$ , the bathymetry changes from a uniform flatness (hereafter *offshore* region) to a uniform slope. This slope continues until the storm surge depth  $h_s$  is reached, upon which the bathymetry returns to a uniform flatness (hereafter *inshore* region) for the rest of the domain, representing the area for storm surge. We set the problem by considering a solitary wave of amplitude  $a_0$ , traveling in the  $x$  direction over a uniform water depth of  $h_0$ , as illustrated in Fig. 2. A negative storm surge depth  $h_s$  corresponds to an inshore region which is elevated above the undisturbed water level. The wave may break either over the sloped transition or over the inshore region. The latter case can occur only for positive inshore depths  $h_s$ , while the former case can occur for  $h_s$  of any sign.

We use the depth  $h_0$  to set the length scale. We set a reference velocity scale using the linear speed  $c_0 = \sqrt{gh_0}$  and find the solitary wave phase speed to be  $c/c_0 = \sqrt{1 + a_0/h_0}$ . The timescale is then set as  $t_0 = \sqrt{h_0/g}$ . We use the Bond number,  $\text{Bo} = \rho gh_0^2/\sigma = 1000$ , to set the surface tension, and the Reynolds number,  $\text{Re} = c_0 h_0/\nu = 40\,000$ , to set the water kinematic viscosity. A ratio of air density to water density of  $\rho_{\text{air}}/\rho = 1/850$  is used. The chosen value of  $\text{Re}$  corresponds with a depth of  $h_0 = 5.46$  cm, and  $\text{Bo}$  with a depth of 8.6 cm for water and air at room temperature. Following evidence from studies of short (deep-water) waves [33–35], we expect these values of  $\text{Re}$  and  $\text{Bo}$  to be asymptotically large, and thus that the essential dynamics of the wave propagation and breaking problem are insensitive to them. Specifically, we expect the speed and rate of steepening of the wave to be insensitive to  $\text{Re}$  and  $\text{Bo}$ , consistent with the findings of Mostert and Deike [20], who validated their numerical data partly against the experiments of Camfield and Street [11,12], which were run at different values of these parameters. The shape of the overturning wave and the local turbulent dissipation rate is also expected to remain insensitive to these values, given observations in deep water [33–35]. To keep the numerical simulations tractable, we therefore do not vary these parameters in the present study, but this assumption remains to be confirmed for shallow-water contexts in future work.

The wave is initialized using the exact soliton solution to the Green-Naghdi equations [58] given by

$$\eta(x) = a_0 \text{sech}^2 \left[ (x - x_w) \sqrt{\frac{3a_0}{4h_0^3} \left( \frac{1 + a_0}{h_0} \right)} \right], \quad (7)$$

$$u_x(x) = \frac{c\eta(x)}{h_0 + \eta(x)}, \quad u_y(x, y) = \frac{c(y + h_0)}{h_0 + \eta(x)} \frac{\partial \eta}{\partial x} \left( 1 - \frac{\eta}{h_0 + \eta_0} \right). \quad (8)$$

This forms a solitary wave, at location  $x_w$  in Fig. 2, that propagates inshore towards the beach, steepens, and breaks, as described in Sec. IV A.

In this study, 123 cases are simulated by varying the three parameters, which are the storm surge depth  $h_s$ , the beach slope  $\alpha \equiv \tan \theta$ , and the offshore wave amplitude  $a_0$ , as illustrated in Table II. For each combination of initial wave amplitude and beach slope, cases are run covering inshore depths from  $h_s/h_0 = -0.4$  to 0.5. Cases with negative storm surge depths represent bathymetry where the inshore region is above the water initially, causing the wave to break against the beach slope. This case is somewhat similar to the bathymetry condition considered in [20], which could be interpreted as the limiting case  $h_s/h_0 \rightarrow -\infty$ .

TABLE II. Outline of the simulated cases. The varying parameters are the beach slope  $\alpha \equiv \tan \theta$  (rows) and offshore wave amplitude  $a_0$  (columns). Note that the beach slope ranges fall under the small angle approximation,  $\alpha \approx \theta$ . The individual entries mark the number of different storm surge (inshore) depths that have been run for the corresponding values of  $a_0$ ,  $\theta$ ; these vary from  $h_s/h_0 = -0.4$  to 0.5.

$\theta \backslash a_0/h_0$	0.2	0.3	0.4	0.5
$2^\circ$	7	8	8	8
$3^\circ$	7	8	8	8
$4^\circ$	7	8	8	7
$5^\circ$	7	8	8	8

## IV. RESULTS AND DISCUSSION

### A. Describing the wave-breaking process

This section discusses the wave breaking process for some representative cases, in which different types of breakers are formed, as illustrated in Figs. 3–5. Figure 3 presents the vorticity around the wave in water at four representative time instants during wave breaking for a case with a positive storm surge depth. For this case the beach slope is  $\theta = 4^\circ$ , the initial wave amplitude is  $a_0/h_0 = 0.4$ , and the storm surge (inshore) depth is  $h_s/h_0 = 0.2$ . The wave begins to break around the boundary between the uniform slope and inshore region [see Fig. 3(a)]; as the wave propagates further, an air cavity forms inside the breaker [see Fig. 3(d)], which is characteristic of a plunging breaker. An additional plunging breaker with a negative storm surge depth is described in Appendix B (see Fig. 11).

Figure 4 shows a case with a large storm surge depth. Here the beach slope is  $\theta = 3^\circ$ , the initial wave amplitude is  $a_0/h_0 = 0.3$ , and the storm surge depth is  $h_s/h_0 = 0.5$ . Similar to Fig. 3, the wave breaks on the inshore region, but no clear air cavity is encapsulated as the wave breaks, and thus this is a spilling breaker.

Finally, Fig. 5 shows a case with a large beach slope. Here the beach slope is  $\theta = 5^\circ$ , the initial wave amplitude is  $a_0/h_0 = 0.4$ , and the storm surge depth is  $h_s/h_0 = -0.4$ , i.e., the inshore region lies well above the undisturbed water level. The wave breaks on the beach slope. From Fig. 5(d), an air pocket is observed, indicating that a plunging breaker is formed.

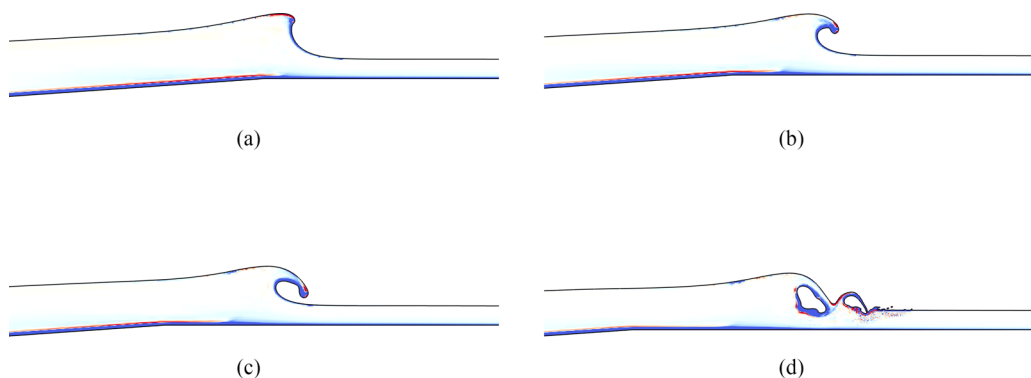


FIG. 3. Wave breaking process (plunging breaker) for the case with a beach slope of  $4^\circ$ , initial wave amplitude of 0.4, and storm surge depth of 0.2. Vorticity (color contour) in the water phase at the following four time instants: (a)  $t/t_0 = 13.8$ , (b)  $t/t_0 = 14.4$ , (c)  $t/t_0 = 14.7$ , (d)  $t/t_0 = 15.3$ .

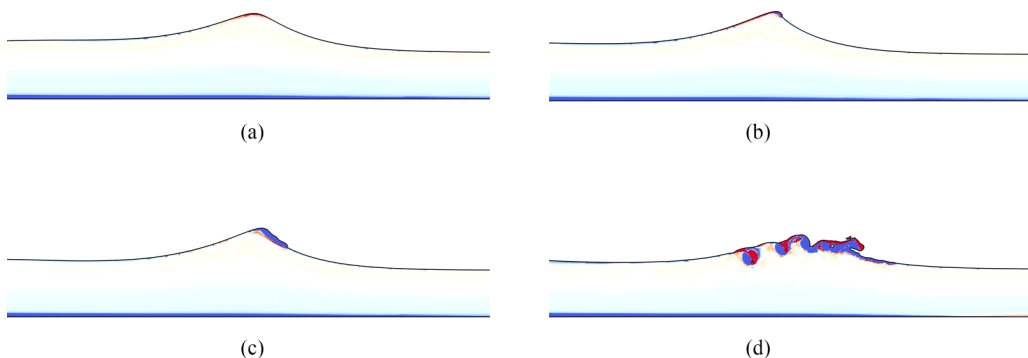


FIG. 4. Wave breaking process (spilling breaker) for the case with a beach slope of  $3^\circ$ , initial wave amplitude of 0.3, and storm surge depth of 0.5. Vorticity (color contour) in the water phase at the following four time instants: (a)  $t/t_0 = 19.75$ , (b)  $t/t_0 = 21.75$ , (c)  $t/t_0 = 23.2$ , and (d)  $t/t_0 = 26.0$ .

In summary, plunging breakers exhibit clear overturning jets, such as those visible in Figs. 3(b), 3(c), 5(b), 5(c), and 11(c); Although spilling breakers also feature overturning behavior, which is essentially the same process as in plungers albeit on smaller length scales [16,33,59], this is not easily distinguishable in the present simulations.

### B. Classifying the types of breakers for all simulation cases

The breakers for all simulation cases are classified as either plunging breakers or spilling breakers. Plunging breakers are characterized by the presence of a well-defined cavity underneath the overturning jet, while spilling breakers in this data set correspond to any other breaking morphology. We note that there is no fundamental difference between plunging and spilling breakers. New *et al.* [60] observed that spilling breakers overturned in a remarkably similar manner to plunging breakers, where the scale of the overturning jet is merely smaller. The same phenomenon was observed in the context of solitary waves specifically [16]. (The similarity does break down for sufficiently small wavelengths, in which case parasitic capillary waves can arise and modify the breaking process [33,61], but this phenomenon occurs for Bond numbers significantly smaller than those considered in the present study and is not qualitatively apparent in our simulations.) Nevertheless, plunging

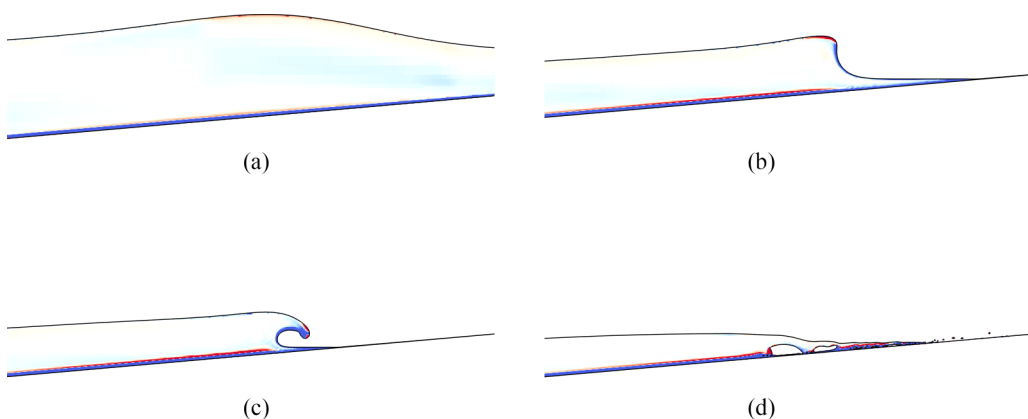


FIG. 5. Wave breaking process (plunging breaker) for the case with a beach slope of  $5^\circ$ , initial wave amplitude of 0.4, and storm surge depth of  $-0.4$ . Vorticity (color contour) in the water phase at the following four time instants: (a)  $t/t_0 = 7.25$ , (b)  $t/t_0 = 12.25$ , (c)  $t/t_0 = 13.2$ , and (d)  $t/t_0 = 14.45$ .



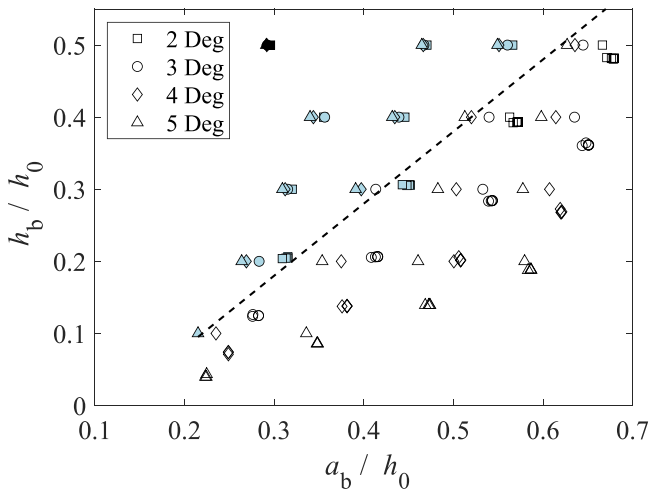


FIG. 6. Breaker types of all simulated cases. Blue-filled shapes represent spilling breakers, and hollow shapes represent plunging breakers. Black-filled shapes at locations of maximum local wave height represent nonbreaking cases. The dashed line ( $h_b = a_b - 0.12$ ) separates the spilling breaking cases from the plunging breaking cases.

breakers as we have defined them here are known to cause significantly increased loadings on offshore structures owing to the presence of the entrained air cavity [62], and the entrained cavity can also affect the wave's dissipative properties [34,35]. It therefore remains of interest to identify this broad change in wave character. To determine whether the type of breaker can be determined by the local conditions of the wave at the moment of breaking, the wave amplitude at breaking  $a_b$  and water depth  $h_b$  under the breaking wave is extracted from the data for each case and normalized by  $h_0$  to get dimensionless wave amplitude  $a_b/h_0$  and water depth  $h_b/h_0$ . The breaking amplitude is then plotted against breaking depth ( $a_b/h_0$ ,  $h_b/h_0$ ) as shown in Fig. 6, with solid and hollow markers denoting spilling and plunging breakers, respectively. The shape of the marker denotes the beach slope. The solid markers and the hollow markers can be separated by a line, which is governed by  $h_b/h_0 = a_b/h_0 - 0.12$  (i.e.,  $a_b/h_b \simeq \text{const}$ ) as indicated by the dashed line in Fig. 6. Given that plunging and spilling breakers are governed by the same overturning behavior, though at different length scales [16,33,59], the particular form of this separating line does not reflect a change in fundamental physical processes, but may instead suggest that breaker intensity correlates with the so-called breaking index  $\gamma \equiv a_b/h_b$ , which is equivalent to one form of the nonlinearity parameter  $F$  (see Sec. IV D). Further, Fig. 6 suggests that, first, breaking amplitude and depth are rather insensitive to beach slope, second, for a given breaking depth, plunging breakers have larger amplitudes than spilling breakers. Putting it another way, if the wave amplitude at breaking is relatively larger, it will have a higher chance to encapsulate air and thus will more likely form a plunging breaker. Third, for sufficiently low wave amplitude and sufficiently high depth, a wave will not break, as indicated by the solid black markers. This threshold is suggested by Losada *et al.* to be  $a_b/h_b = 0.7$ , for example [21].

### C. Determining energy budget and dissipation

For all the simulated cases, the energy dissipation is examined. Figure 7 shows the energy dissipation process for a few representative cases, namely, with storm surge (inshore) depths of  $h_s/h_0 = -0.2, 0.1, 0.3$ , and  $-0.4$ , respectively.

In the figures, the dotted line represents the gravitational potential energy, the dashed line represents the kinetic energy, and the dark line represents the sum of these two, as the total conservative

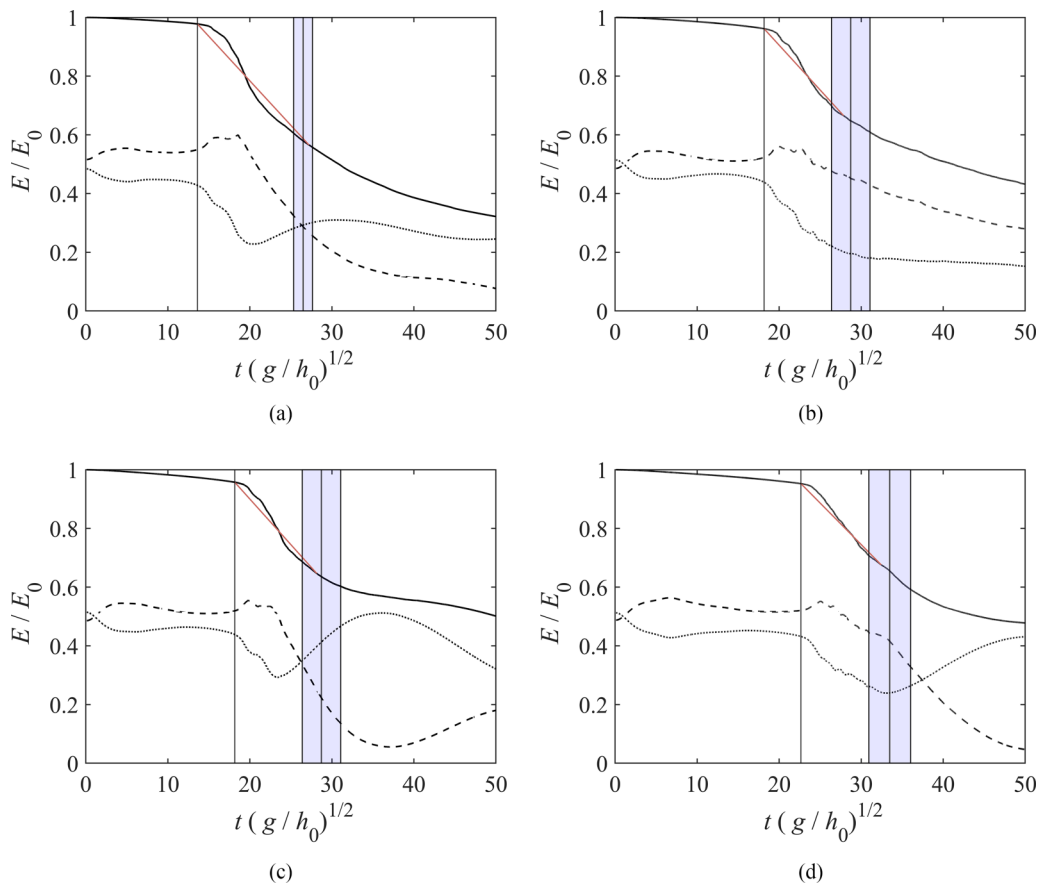


FIG. 7. Energy dissipation for representative cases: (a) 0.5 amplitude,  $3^\circ$  beach slope,  $-0.2$  storm surge depth; (b) 0.3 amplitude,  $3^\circ$  beach slope,  $0.1$  storm surge depth; (c) 0.3 amplitude,  $3^\circ$  beach slope,  $-0.4$  storm surge depth; and (d) 0.3 amplitude,  $2^\circ$  beach slope,  $-0.4$  storm surge depth. Kinetic energy is shown as the dashed line, gravitational potential energy is shown as the dotted line, and total energy is shown as the solid line. The leftmost vertical line represents the start of breaking time, while the three rightmost vertical lines represent the error bar approximation of breaking end time. The solid red line represents the line of best fit for the specific total energy dissipation curve.

energy. (The surface tension energy has been found in such cases to be negligible [20,33]). The leftmost vertical line represents the time when the wave begins to break (namely, when the wave face becomes vertical). The natural end time of breaking, however, is not immediately obvious. In [20] the end time was defined as the moment after breaking that the gravitational potential and kinetic energies were equal; this corresponds to the crossover of these energies in the case of Fig. 7(a), which has a negative storm surge depth and thus the wave breaks on the beach slope. This is due to the transfer of kinetic energy to gravitational potential energy as the wave runs up the beach. In such a case, the wave exchanges kinetic energy that would otherwise be available for dissipation through breaking into gravitational potential energy, which rapidly slows or terminates the breaking process. However, such a moment does not arise naturally for cases with positive storm surge depths or for small negative storm surge depths in the present study. This is because for such cases, the breaker cannot gain a significant amount of gravitational potential through runup; it thus retains kinetic energy available for dissipation, allowing the breaking process to prolong without a clear endpoint. Therefore, in this study, an approach to determining the breaking end time is developed using a

linear regression of the total energy budget, as shown in Fig. 7. First, in our analysis, we consider a parameter sweep to be a series of cases of varying storm surge depth ( $h_s/h_0 = -0.4-0.5$ ) with the same combination of beach slope ( $\theta$ ) and initial wave amplitude ( $a_0$ ), as shown in Table II. For each combination of ( $a_0/h_0$ ,  $\theta$ ,  $h_s/h_0$ ), a least-squares line is fit to the energy budget from the breaking time  $t_1 = t_b$  to a range of candidates for the end time  $t_2$ . The candidate of  $t_2$  resulting in the best fit (i.e., with the highest determination coefficient  $R^2$ ) is noted. For a given combination of ( $a_0/h_0$ ,  $\theta$ ), the results are then averaged into a single end breaking time, across the set of all corresponding storm surge depths. The range of best end breaking times within this set is used to develop error bars for the dissipation rate at each storm surge depth. While all the cases at a given ( $a_0/h_0$ ,  $\theta$ ) share the same temporal distance between the start and end of breaking, each case will have distinct error bars for energy dissipation rate since the energy budget is unique for each case.

Results for some representative cases are shown in Fig. 7. The red line in each figure shows a linear fit between  $t_1 = t_b$  and the candidate  $t_2$  with the highest  $R^2$  value for that case; the three rightmost vertical lines in the shaded region represent the end time of the breaking event with the center line representing the average breaking end time across all storm surge depths at the given ( $a_0/h_0$ ,  $\theta$ ), and the left and right lines representing the error bar range. From all figures, a clear drop in total energy is observed as the wave breaks. The cases with negative storm surge depths show a steep drop in kinetic energy when compared to those with positive storm surge depths, due to wave breaking on the beach slope, which reduces the water velocity more significantly. For all cases, the initial energy dissipation observed in the wave before breaking is a physical effect captured by the numerical simulations and is numerically converged in our study.

Figure 7(a) shows that for negative storm surge depths, this method can predict a breaking end time very close to the crossover point between kinetic and gravitational potential energy used in [20], without any additional tuning of parameters, although we note that this behavior is not observed in all cases. While the kinetic or gravitational crossover often lies within the range of best  $t_2$  within a given set of storm surge depths [as in Fig. 7(c)], this is not always guaranteed [Fig. 7(d)].

#### D. Characterizing dissipation rate

The energy dissipation induced by a breaking wave is typically described by its dissipation rate per unit length of breaking crest,  $\epsilon_l$  [39]. In this study the dissipation rate is determined using a linear fit to the total energy (i.e., the sum of gravitational potential and kinetic energies) during the breaking event,

$$\epsilon_l = \frac{\Delta E}{\Delta t}, \quad (9)$$

where  $\Delta E = |E_1 - E_2|$  and  $\Delta t = |t_1 - t_2|$ , with subscripts 1 and 2 representing the start and end of the breaking event, respectively. Aside from how  $t_2$  is determined (see Sec. IV C), this is consistent with the methodology applied in [20,35]. The dissipation rates for all simulation cases are shown in Fig. 8.

Figure 8(a) plots the dissipation rates against normalized  $a_b$  for all the simulated cases. The colors of black, red, green, and blue represent beach slopes of  $\theta = 2^\circ, 3^\circ, 4^\circ$ , and  $5^\circ$ , respectively. Scaled dissipation rate is plotted with respect to the local breaking conditions, where the constant,  $\epsilon_0 = \rho g^{3/2} h_0^{5/2}$ , is used to normalize the dissipation rate. Error bars are included for each data point to calculate the dissipation rate at the upper and lower limits of the end breaking time as described in Sec. IV C. The dissipation rate from [20] is also included in Fig. 8(a) for comparison, shown as hollow squares. In general, across all cases the dissipation rate increases with the wave amplitude at breaking, but there is considerable variation in the data due to the effects of the beach slope and inshore storm surge depth. Note that despite the methodological differences, the estimates for the dissipation rate for negative storm surge depths in the present data lie approximately within the spread of the cited data from [20], which corresponds to the limit  $h_s/h_0 \rightarrow -\infty$ .

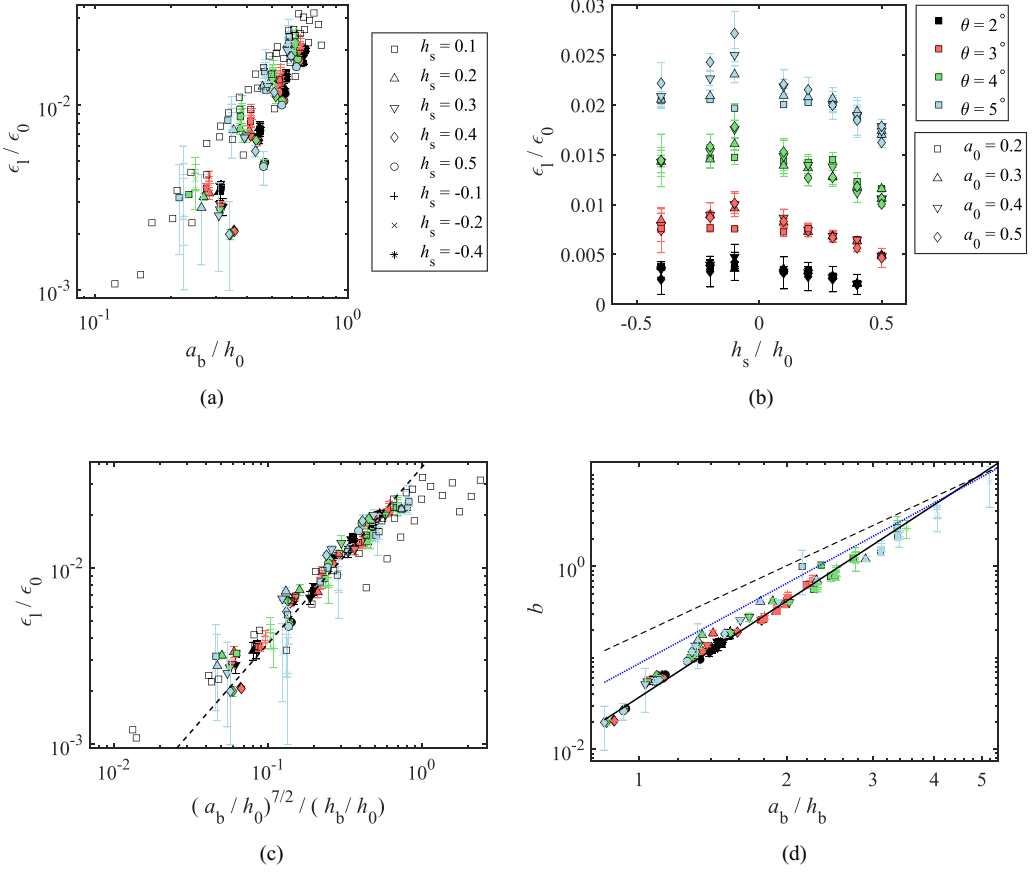


FIG. 8. (a) Dissipation rate plotted against normalized wave amplitude at breaking for all simulated cases. Data from [20] are also included as hollow squares for comparison. (b) Dissipation rate plotted against storm surge depth. (c) Dissipation rate plotted against  $a_b$  scaled by  $h_b$ . The line represents the shallow water inertial model from [20]. (d) Breaking parameter shown in Eq. (1) plotted against nonlinearity parameter  $a_b/h_b$ . Dashed and solid lines represent deep- and shallow-water scalings, respectively. Blue dotted line represents the hydraulic jump bore model [43]. For panels (c) and (d), shape representation is as shown in (a), and for all panels, color representation is as shown in panel (b).

Figure 8(b) shows dissipation rate plotted against storm surge depth for all simulation cases. Clear delineations can be seen between the cases of the various beach slopes. The cases with higher beach slopes tend to experience a higher dissipation rate. Overall, for the cases with positive storm surge depths, the dissipation rate decreases with increasing storm surge depth. This is because for positive  $h_s/h_0$ , the wave can break either on the slope ( $h_b > h_s$ ) or on the inshore region ( $h_b = h_s$ ); hence, following the inertial argument of Sec. II, the integral length scales of the turbulence can only increase with increasing  $h_s/h_0$ , corresponding with lower dissipation rates. On the other hand, for the cases with negative storm surge depths, dissipation rate decreases with increasing  $|h_s/h_0|$ , i.e., with increasing elevation difference between the inshore region and the undisturbed water level, and the greatest energy dissipation rate occurs where the inshore region is at only slightly higher elevation than the water level. While all waves with negative  $h_s/h_0$  break on the sloped region, the resulting runup forces the integral length scales of the turbulent flow to reduce, driving an increase in dissipation rate. This effect is strong for small  $|h_s/h_0|$ . However, for large negative values of  $h_s/h_0$ , the breaker runs up the slope and thereby rapidly exchanges kinetic energy for gravitational

potential energy, so that there is less available energy for dissipation. This effect appears to outstrip the increase in dissipation rate resulting from the smaller integral length scales and results in a lower dissipation rate. Note finally that the negative values of  $h_s/h_0$  tend to show slightly larger error bars than for positive  $h_s/h_0$ ; these indicate greater variability in the energy budget between different slopes and wave amplitudes for a given storm surge depth.

We now examine the performance of different parametrizations in capturing the trends in the data. Figure 8(c) shows the energy dissipation rates scaled according to Eq. (5), i.e., the shallow-water parametrization of [20]. The data collapse consistently with the scaling, represented by the dashed line in the figure. For small dissipation rates and high beach slopes, the data with negative  $h_s/h_0$  tend to show the greatest relative deviation from the scaling (in addition to having large error bars). This reflects that as the wave runs up the beach, the inertial argument that leads to Eq. (5) becomes less relevant because the breaking depth  $h_b$  is no longer properly defined. Moreover, as the breaker runs up the beach, dissipation due to the bottom boundary layer may become significant; such effects are not accounted for in Eq. (5). These observations also apply to the DNS data of [20] and may explain why it does not fully collapse to the parametrization.

We compare other parametrizations in Fig. 8(d), making use of the nonlinearity parameter of [63] and [64],

$$F = \frac{ga^2}{c^2}, \quad (10)$$

where  $a$  is a representative amplitude and  $c$  is a phase speed. In the shallow-water limit, with  $c = \sqrt{gh_b}$ , we have  $F \rightarrow a_b/h_b$ . We also explicitly use the dimensionless breaking parameter  $b$  defined in Eq. (1), which is especially relevant to deep-water studies [39,46], but can also be defined for shallow water (see Sec. II). With  $c = \sqrt{gh_b}$ , the shallow water scaling [Eq. (5) of [20]] can be nondimensionalized into  $b \propto F^{7/2}$ , and is shown with the solid line. In the deep-water limit (i.e., the context of [46]),  $F \rightarrow S$  where  $S$  is the breaking slope, obtaining  $b \propto F^{5/2}$ . Note that the inertial argument of [46] can apply to any breaker, provided the integral length scale of the turbulence can be approximated by  $a_b$  (rather than  $h_b$ , as in [20]), which could occur in the shallow-water limit for cases where  $a_b/h_b \geq 1$ , which is common in the present data. Even in this case, however, the scaling  $b \propto F^{5/2}$  is recovered. This is shown by the dashed line. Finally, the dimensionless form of the bore model (2) yields

$$b = \beta F^3 \left( \frac{2+F}{2+2F} \right)^{1/2} \quad (11)$$

and is shown with the blue dotted line. This model relies on the assumption that all waves in shallow water can be energetically modeled as hydraulic jumps. When plotted together, the data obtained in this study appear to best match the inertial scaling in Eq. (5) of [20]. The other scalings have shallower slopes, with the deep water scaling deviating most from the data obtained in this study.

### E. Considerations for a general breaking parametrization

We have found that for solitary waves in the presence of a simple storm surge geometry, the shallow-water parametrization  $b \propto F^{7/2}$  of [20] predicts well the dissipation rate of breaking. It better collapses the DNS data of the present study than for the hydraulic jump model, Eq. (2), suggesting that solitary waves are not well approximated energetically by hydraulic jumps. However, the shallow-water parametrization  $F^{7/2}$  performs better even for breakers where  $a_b > h_b$ , equivalently  $F > 1$ , for which one might expect that the parametrization  $b \propto F^{5/2}$  of [46] would be superior. We therefore discuss now briefly whether these two parametrizations could be harmonized across different data sets, including both shallow- and deep-water regimes.

Note the nonlinearity parameter  $F$  in Eq. (10) can be used to nondimensionalize the water wave equations in a depth-independent way. Using the linear phase speed in arbitrary depth,  $c^2 = (g/k) \tanh(kh)$ , in the short-wave (deep-water) limit,  $F \sim ak = S$  is the wave slope, while

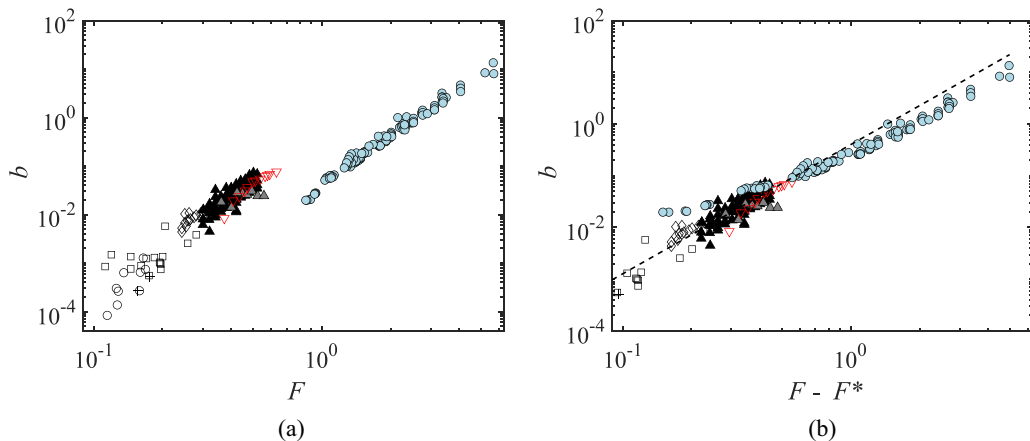


FIG. 9. (a) Plot of  $b$  parameter against nonlinearity parameter  $F$  for shallow-water data from the present study and deep-water data from literature. Black and gray triangles and gray diamonds are from Drazen *et al.* [46]; cross and circles from Banner and Peirson [65]; squares from Grare *et al.* [66]; red triangles are DNS from Deike *et al.* [33]. Blue circles are the present shallow-water DNS. (a) Data plotted without shifts or scaling, (b) Data shifted horizontally by estimated breaking threshold  $F^*$ . For the deep-water data,  $F^* = 0.08$ ; for the present shallow-water DNS data,  $F^* = 0.7$ .

in the long-wave (shallow-water) limit,  $F \sim a/h$ . Figure 9(a) shows the  $b$  parameter for a variety of experimental and numerical sources for deep-water breakers ([33,34,46,65,66]), along with the present shallow-water data set. While the shallow-water data set appears to have a slope qualitatively similar to the deep-water data, there is a clear break between the two groups, and a single power-law scaling cannot capture both data sets.

The difference may possibly be accommodated with a heuristic consideration of breaking threshold. In their semiempirical study, [47] fitted a best-fit curve to deep-water data, finding

$$b = 0.4(S - S_T)^{5/2}, \quad (12)$$

with  $S_T = 0.08$ . Here  $S_T$  can be qualitatively interpreted as a breaking threshold, which is closely related to questions of breaking dissipation. Identifying breaking criteria in deep and shallow water remains an active research topic ([33,46,50–52,67–69]), and recent investigations have shown that the breaking criterion in deep water depends on the bandwidth of the breaking wave group, somewhat equivalent to a Benjamin-Feir index ([50,51,69]). It is not the purpose of this study to speculate on the breaking threshold for shoaling solitary waves, and breaker bandwidth is not well defined for these waves, but we may give a rough heuristic estimate of  $F^* \simeq 0.7$ , following Losada *et al.* [21] who found this threshold for solitary waves encountering abrupt depth changes. Plotting then a modified fit  $b = 0.4(F - F^*)^{5/2}$  with  $F^* = 0.08$  in deep water, and  $F^* = 0.7$  in shallow water, produces Fig. 9(b), which more closely collapses the deep- and shallow-water data.

While promising, the above approach, and indeed the comparison of different parametrizations in Sec. IV D, essentially sets  $F = a_b/h_b$ , well known as the breaking index  $\gamma$  ([70]), but it relies on identifying the crest speed with the linear wave speed at the breaking depth,  $c = \sqrt{gh_b}$ . However, the breaking crest in fact remains close to its offshore speed,  $c_0 = \sqrt{g(h_0 + a_0)} \simeq \sqrt{gh_0}$ , which is a more natural choice for nondimensionalizing the energy dissipation. Using it actually identifies the  $b$  parameter with the left-hand side of Eq. (4), since  $g^{3/2}h_0^{5/2} = c_0^5/g$ , in which case we can interpret Eq. (4) as

$$b_0 = \beta F_0^{7/2} M^2 = \beta F_0^{5/2} \gamma, \quad (13)$$

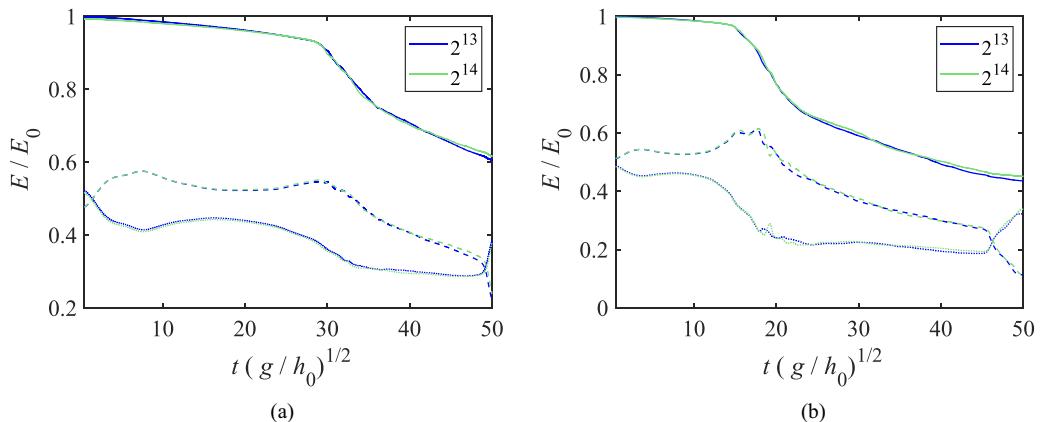


FIG. 10. Comparison of energy budget between two mesh resolution levels  $2^{13}$  and  $2^{14}$  for two cases: (a) 0.2 initial wave amplitude,  $2^\circ$  beach slope, and 0.3 storm surge depth; (b) 0.4 initial wave amplitude,  $4^\circ$  beach slope, and 0.3 storm surge depth.

where  $b_0 = g\epsilon/(\rho c_0^5)$ ,  $F_0 = a_b/h_0$ , and  $M^2 = c_0/c = h_0/h_b$  is the ratio of the inshore and offshore wave speeds, and  $\gamma$  is the breaking index. The second of Eq. (13) is suggestive of a close link with the deep-water scaling [46], except that  $\gamma$  (and  $M^2$ ) do not have deep-water equivalents, so that they cannot be immediately compared on the same axes.

We remark finally that the dynamic/kinematic parametrization of [18] using the parameter  $\Gamma$  has shown good data collapse, but  $\Gamma$  is difficult to estimate for the present data owing to noise in the numerical differentiation of the related quantity  $u_x/c$ , evaluated at the wave crest.

## V. CONCLUSIONS

In this study, we have conducted various two-dimensional direct-numerical simulations of solitary wave breaking over a simple storm surge bathymetry, varying the depth of the storm surge, beach slope, and wave initial amplitude. The resulting breakers can be classified into plunging or spilling breakers through a clear separation line, which was developed based on wave amplitude and water depth at the point of breaking. In addition, we studied the energy dissipation of the cases to determine a dissipation rate for each case. Comparing with prior dissipation rate data from the literature, we found that the shallow water dissipation rate model developed in [20] can be extended to this storm-surge-style bathymetry with good data collapse, performing better than the hydraulic jump analogy or the deep-water parametrization of [46]. Furthermore, we compared our shallow water data with deep water data from literature using a breaking parameter and explored possibilities of a unifying model. A promising collapse of most of the data can be obtained. The obtained results from this paper could in the future be used to study how changes in the energy dissipation of breaking waves affect the wave loading on coastal structures, particularly in the presence of a storm surge. Possibilities for implementing the parametrization of Mostert and Deike [20] into a Boussinesq-type or other regional-scale wave-resolving model will also be explored in a future study.

## ACKNOWLEDGMENTS

Numerical simulations in this study were performed using the Foundry cluster at Missouri University of Science and Technology, which is supported by the National Science Foundation under Grant No. OAC-1919789. H.B. and G.Y. appreciate the financial support from the Mid-American Transportation Center, through the MATC project starting in 2021, ‘‘Understanding of Bridge

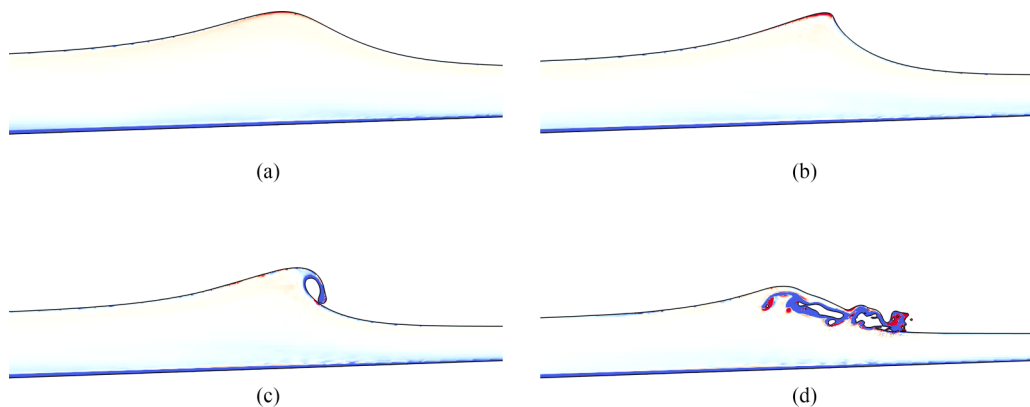


FIG. 11. Wave breaking process (plunging breaker) for the case with a beach slope of  $2^\circ$ , an initial wave amplitude of 0.5, and a storm surge depth of  $-0.1$ . Vorticity (color contour) in the water phase at the following four time instants: (a)  $t/t_0 = 13.2$ , (b)  $t/t_0 = 15.6$ , (c)  $t/t_0 = 17.2$ , and (d)  $t/t_0 = 19.0$ .

Vulnerability to Climate Change Enables Pro-active Adaptation Measures,” as well as National Science Foundation Grant CoPe Eager. W.M. gratefully acknowledges support from a University of Oxford startup fund.

#### APPENDIX A: CONVERGENCE STUDY

The meshes used for these simulations are square, such that  $\Delta x = \Delta y$ . Our choice of mesh size is related to the numerical convergence. We follow the process used in [20] to measure the numerical convergence based on the energy budget. The kinetic and gravitational potential energies,  $E_k$  and  $E_p$ , are

$$E_k = \frac{1}{2} \int_V \rho |\mathbf{u} \cdot \mathbf{u}| dV, \quad E_p = \int_V \rho g y dV - E_{p0}, \quad E = E_k + E_p. \quad (\text{A1})$$

In Fig. 10, we show a comparison of energy budget convergence for two cases: one with a  $2^\circ$  beach slope and 0.2 initial wave amplitude, and one with  $4^\circ$  beach slope and 0.4 initial wave amplitude. Both cases have a storm surge depth of 0.3. In both cases, we compare mesh sizes of  $\Delta x = L_0/2^{13}$  and  $\Delta x = L_0/2^{14}$ , where  $L_0$  is the length of the domain. We see that there is little difference between the energy dissipation between the two resolutions and thus conclude that these simulations converge for a resolution of  $2^{13}$ .

#### APPENDIX B: ADDITIONAL BREAKER INTERFACE PLOTS

Figure 11 shows a case with a negative storm surge depth. Here the beach slope is  $\theta = 2^\circ$ , the initial wave amplitude is  $a_0/h_0 = 0.5$ , and the storm surge depth is  $h_s/h_0 = -0.1$ , i.e., the inshore region lies above the undisturbed water level. In this case the wave breaks on the beach slope. The air cavities observed in Fig. 11(d) again indicate that this is a plunging breaker. This behavior is similar to the cases presented in [20], in which the bathymetry does not include an inshore region, so that the wave breaks directly on the beach slope.

---

[1] N. Elko, F. Feddersen, D. Foster, C. Hapke, J. McNinch, R. Mulligan, H. T. Özkan-Haller, N. Plant, and B. Raubenheimer, The future of nearshore processes research, *Shore Beach* **83**, 13 (2015).



- [2] W. K. Melville, The role of surface-wave breaking in air-sea interaction, *Annu. Rev. Fluid Mech.* **28**, 279 (1996).
- [3] J. Battjes, Surf-zone dynamics, *Annu. Rev. Fluid Mech.* **20**, 257 (1988).
- [4] F. Feddersen and J. Trowbridge, The effect of wave breaking on surf-zone turbulence and alongshore currents: A modeling study, *J. Phys. Oceanogr.* **35**, 2187 (2005).
- [5] M. Moulton, S. H. Suanda, J. C. Garwood, N. Kumar, M. R. Fewings, and J. M. Pringle, Exchange of plankton, pollutants, and particles across the nearshore region, *Annu. Rev. Marine Sci.* **15**, 167 (2022).
- [6] U. S. Army Corps of Engineers, Coastal engineering manual, Engineering Manual, No. 1110-2-1100 (USACE Publications, 2002).
- [7] X. Wu, F. Feddersen, and S. N. Giddings, Diagnosing surfzone impacts on inner-shelf flow spatial variability using realistic model experiments with and without surface gravity waves, *J. Phys. Oceanogr.* **51**, 2505 (2021).
- [8] R. Guza and F. Feddersen, Effect of wave frequency and directional spread on shoreline runup, *Geophys. Res. Lett.* **39**, L11607 (2012).
- [9] F. Feddersen, Observations of the surf-zone turbulent dissipation rate, *J. Phys. Oceanogr.* **42**, 386 (2012).
- [10] E. G. Bautista, E. Arcos, and O. E. Bautista, Propagation of ocean waves over a shelf with linear transition, *Mec. Comput.* 225 (2011).
- [11] F. E. Camfield and R. L. Street, The effects of bottom configuration on the deformation, breaking and run-up of solitary waves, in *11th Intl. Conf. on Coastal Engineering* (ASCE, Reston, VA, 1969), p. 173.
- [12] F. E. Camfield and R. L. Street, Shoaling of solitary waves on small slopes, *J. Wtrwy Harb. Div.* **95**, 1 (1969).
- [13] C. E. Synolakis, The runup of solitary waves, *J. Fluid Mech.* **185**, 523 (1987).
- [14] J. Skjelbreia, Observation of breaking waves on beaches by use of an LDV, Ph.D. thesis, California Institute of Technology (1987).
- [15] S. T. Grilli, M. A. Losada, and F. Martin, Characteristics of solitary wave breaking induced by breakwaters, *J. Wtrwy Port Coastal Ocean Eng.* **120**, 74 (1994).
- [16] S. T. Grilli, I. A. Svendsen, and R. Subramanya, Breaking criterion and characteristics for solitary waves on slopes, *J. Wtrwy Port Coastal Ocean Eng.* **123**, 102 (1997).
- [17] Y. Li and F. Raichlen, Non-breaking and breaking solitary wave run-up, *J. Fluid Mech.* **456**, 295 (2002).
- [18] M. Derakhti, M. L. Banner, and J. T. Kirby, Predicting the breaking strength of gravity water waves in deep and intermediate depth, *J. Fluid Mech.* **848**, R2 (2018).
- [19] S. T. Grilli, J. Horrillo, and S. Guignard, Fully nonlinear potential flow simulations of wave shoaling over slopes: Spilling breaker model and integral wave properties, *Water Waves* **2**, 263 (2020).
- [20] W. Mostert and L. Deike, Inertial energy dissipation in shallow-water breaking waves, *J. Fluid Mech.* **890**, A12 (2020).
- [21] M. Losada, C. Vidal, and R. Medina, Experimental study of the evolution of a solitary wave at an abrupt junction, *J. Geophys. Res. Oceans* **94**, 14557 (1989).
- [22] D. G. Goring and F. Raichlen, Propagation of long waves onto shelf, *J. Wtrwy Port Coastal Ocean Eng.* **118**, 43 (1992).
- [23] A. Giniyatullin, A. Kurkin, S. Semin, and Y. A. Stepanyants, Transformation of narrowband wavetrains of surface gravity waves passing over a bottom step, *Math. Model. Nat. Phenom.* **9**, 73 (2014).
- [24] I. Gorban, A numerical study of solitary wave interactions with a bottom step, in *Continuous and Distributed Systems II*, edited by Viktor A. Sadovnichiy and Mikhail Z. Zgurovsky (Springer, Cham, Switzerland, 2015), pp. 369–387.
- [25] A. Kurkin, S. Semin, and Y. A. Stepanyants, Transformation of surface waves over a bottom step, *Izvestiya, Atmos. Oceanic Phys.* **51**, 214 (2015).
- [26] Y. Li, S. Draycott, Y. Zheng, Z. Lin, T. A. Adcock, and T. S. Van Den Bremer, Why rogue waves occur atop abrupt depth transitions, *J. Fluid Mech.* **919**, R5 (2021).
- [27] S. Draycott, Y. Li, P. Stansby, T. Adcock, and T. van den Bremer, Harmonic-induced wave breaking due to abrupt depth transitions: An experimental and numerical study, *Coastal Eng.* **171**, 104041 (2022).
- [28] S. T. Grilli, M. A. Losada, and F. Martin, Wave impact forces on mixed breakwaters, *Coastal Eng. Proc.* 1161 (1992).

- [29] Y. Liu and Y.-c. Li, Wave interaction with a wave absorbing double curtain-wall breakwater, *Ocean Eng.* **38**, 1237 (2011).
- [30] S. Mohanlal, J. Harris, M. Yates, and S. Grilli, Unified depth-limited wave breaking detection and dissipation in fully nonlinear potential flow models, *Coast. Eng.* (2022), doi: [10.1016/j.coastaleng.2023.104316](https://doi.org/10.1016/j.coastaleng.2023.104316).
- [31] C. Song and A. I. Sirviente, A numerical study of breaking waves, *Phys. Fluids* **16**, 2649 (2004).
- [32] N. Emarat, D. I. M. Forehand, E. D. Christensen, and C. A. Greated, Experimental and numerical investigation of the internal kinematics of a surf-zone plunging breaker, *Eur. J. Mech. B Fluids* **32**, 1 (2012).
- [33] L. Deike, S. Popinet, and W. K. Melville, Capillary effects on wave breaking, *J. Fluid Mech.* **769**, 541 (2015).
- [34] L. Deike, W. K. Melville, and S. Popinet, Air entrainment and bubble statistics in breaking waves, *J. Fluid Mech.* **801**, 91 (2016).
- [35] W. Mostert, S. Popinet, and L. Deike, High-resolution direct simulation of deep water breaking waves: Transition to turbulence, bubbles and droplets production, *J. Fluid Mech.* **942**, A27 (2022).
- [36] A. Iafrati, Numerical study of the effects of the breaking intensity on wave breaking flows, *J. Fluid Mech.* **622**, 371 (2009).
- [37] D. H. Peregrine, Surf zone currents, *Theoret. Comput. Fluid Dyn.* **10**, 295 (1998).
- [38] M. Brocchini, A reasoned overview on Boussinesq-type models: the interplay between physics, mathematics and numerics, *Proc. R. Soc. A.* **469**, 20130496 (2013).
- [39] J. H. Duncan, An experimental investigation of breaking waves produced by a towed hydrofoil, *Proc. Royal Soc. A* **377**, 331 (1981).
- [40] J. H. Duncan, A note on the evaluation of the wave resistance of two-dimensional bodies from measurements of the downstream wave profile, *J. Ship Res.* (1982).
- [41] A. B. Kennedy, Q. Chen, J. T. Kirby, and R. A. Dalrymple, Boussinesq modeling of wave transformation, breaking, and runup. I: 1D, *J. Wtrwy Port Coastal Ocean Eng.* **126**, 39 (2000).
- [42] O. M. Phillips, Spectral and statistical properties of the equilibrium range in wind-generated gravity waves, *J. Fluid Mech.* **156**, 505 (1985).
- [43] G. B. Whitham, *Linear and Nonlinear Waves* (Wiley-Interscience, 1999).
- [44] M. Tissier, P. Bonneton, F. Marche, F. Chazel, and D. Lannes, A new approach to handle wave breaking in full non-linear Boussinesq models, *J. Coast. Eng.* **67**, 54 (2012).
- [45] N. Booji, R. C. Ris, and L. H. Holthuijsen, A third-generation wave model for coastal regions 1. Model description and validation, *J. Geophys. Res.* **104**, 7649 (1999).
- [46] D. A. Drazen, W. K. Melville, and L. Lenain, Inertial scaling of dissipation in unsteady breaking waves, *J. Fluid Mech.* **611**, 307 (2008).
- [47] L. Romero, W. K. Melville, and J. M. Kleiss, Spectral energy dissipation due to surface wave breaking, *J. Phys. Oceanogr.* **42**, 1421 (2012).
- [48] L. Romero, Distribution of surface wave breaking fronts, *Geophys. Res. Lett.* **46**, 10463 (2019).
- [49] K. Martins, C. E. Blenkinsopp, R. Deigaard, and H. E. Power, Energy dissipation in the inner surf zone: New insights from LIDAR-based roller geometry measurements, *J. Geophys. Res. Oceans* **123**, 3386 (2018).
- [50] N. Pizzo and W. K. Melville, Focusing deep-water surface gravity wave packets: Wave breaking criterion in a simplified model, *J. Fluid Mech.* **873**, 238 (2019).
- [51] J. T. Sinnis, L. Grare, L. Lenain, and N. Pizzo, Laboratory studies of the role of bandwidth in surface transport and energy dissipation of deep-water breaking waves, *J. Fluid Mech.* **927**, A5 (2021).
- [52] X. Barthelemy, M. Banner, W. Peirson, F. Fedele, M. Allis, and F. Dias, On a unified breaking onset threshold for gravity waves in deep and intermediate depth water, *J. Fluid Mech.* **841**, 463 (2018).
- [53] S. Popinet, Gerris: A tree-based adaptive solver for the incompressible Euler equations in complex geometries, *J. Comput. Phys.* **190**, 572 (2003).
- [54] J. B. Bell, P. Colella, and H. M. Glaz, A second-order projection method for the incompressible Navier-Stokes equations, *J. Comput. Phys.* **85**, 257 (1989).
- [55] S. Popinet, An accurate adaptive solver for surface-tension-driven interfacial flows, *J. Comput. Phys.* **228**, 5838 (2009).

- [56] J. U. Brackbill, D. B. Kothe, and C. Zemach, A continuum method for modeling surface tension, *J. Comput. Phys.* **100**, 335 (1992).
- [57] J. A. Van Hooft, S. Popinet, C. C. Van Heerwaarden, S. J. Van der Linden, S. R. de Roode, and B. J. Van de Wiel, Towards adaptive grids for atmospheric boundary-layer simulations, *Bound.-Layer Meteorol.* **167**, 421 (2018).
- [58] O. L. Métayer, S. Gavriyuk, and S. Hank, A numerical scheme for Green-Naghdi model, *J. Comput. Phys.* **229**, 2034 (2010).
- [59] N. Pizzo and W. K. Melville, Vortex generation by deep-water breaking waves, *J. Fluid Mech.* **734**, 198 (2013).
- [60] A. New, P. McIver, and D. Peregrine, Computations of overturning waves, *J. Fluid Mech.* **150**, 233 (1985).
- [61] J. Duncan, V. Philomin, M. Behres, and J. Kimmel, The formation of spilling breaking water waves, *Phys. Fluids* **6**, 2558 (1994).
- [62] Z. Z. Hu, T. Mai, D. Greaves, and A. Raby, Investigations of offshore breaking wave impacts on a large offshore structure, *J. Fluids Struct.* **75**, 99 (2017).
- [63] J. T. Kirby, Discussion of ‘Note on a nonlinearity parameter of surface waves’ by S. Beji, *J. Coast Eng.* **34**, 163 (1998).
- [64] S. Beji, Note on a nonlinearity parameter of surface waves, *Coast. Eng.* **25**, 81 (1995).
- [65] M. L. Banner and W. L. Peirson, Wave breaking onset and strength for two-dimensional deep water waves groups, *J. Fluid Mech.* **585**, 93 (2007).
- [66] L. Grare, W. L. Peirson, H. Branger, J. W. Walker, J.-P. Giovanangeli, and V. Makin, Growth and dissipation of wind-forced, deep-water waves, *J. Fluid Mech.* **722**, 5 (2013).
- [67] M. Derakhti and J. T. Kirby, Breaking-onset, energy and momentum flux in unsteady focused wave packets, *J. Fluid Mech.* **790**, 553 (2016).
- [68] M. Derakhti, J. T. Kirby, M. L. Banner, S. T. Grilli, and J. Thomson, A unified breaking onset criterion for surface gravity water waves in arbitrary depth, *J. Geo. Phys. Res.: Oceans* **125**, e2019JC015886 (2020).
- [69] N. Pizzo, E. Murray, D. L. Smith, and L. Lenain, The role of bandwidth in setting the breaking slope threshold of deep-water focusing wave packets, *Phys. Fluids* **33**, 111706 (2021).
- [70] B. Robertson, K. Hall, R. Zytner, and I. Nistor, Breaking waves: Review of characteristic relationships, *J. Coast. Eng.* **55**, 1350002-1 (2013).